CDF/ANAL/EXOTIC/CDFR/7616
Version 1.5
November 22, 2005

A Search for High Mass Resonances Decaying to $e\mu$

K. Hahn, N. Lockyer, P. Wittich
University of Pennsylvania

Abstract

We search for high mass, narrow width resonances decaying to $e\mu$ and interpret our results in the context of R-parity violating sneutrino decay and lepton flavor violating Z' decay. Finding no evidence for these processes, we exclude values of the λ_{132} and λ'_{311} RPV coupling constants, the Q^l_{12} $U(1)'$ charge and the Z' c_u and c_d parameters as a function of $e\mu$ invariant mass.

Contents

1 Introduction

We search for high mass resonances decaying directly to an oppositely charged $e\mu$ final state. A number of interesting models of new physics predict decays in this channel. Several classes of theories incorporate Z'_0 bosons that undergo lepton flavor violating (LFV) decays to $e\mu$ [1]. A narrow width $e\mu$ signal is also predicted by Supersymmeteric theories describing the R-parity violating (RPV) decays of heavy neutral particles [2]. Experimental considerations provide additional motivation for the search. A high P_T $e\mu$ signature is attractive due to the lack of competing Standard Model background. The excess of $e\mu$ events found in the combined Run I and II top dilepton analyses[3] is also compelling.

Following an approach taken in Run I, we interpret the results of our search in the context of the RPV production and decay of the tau sneutrino, the scalar superpartner of the neutrino [4]. A general Supersymmetric theory will contain RPV terms that describe lepton and baryon number violating (LNV and BNV) processes. In such processes the coupling strengths of Supersymmetric to Standard Model (SM) particles are given by the "lambda" parameters. The λ_{ijk} and λ'_{ijk} parameters couple SUSY particles to leptons and quarks and result in LNV processes. λ''_{ijk} joins sparticles with baryons and leads to BNV interactions. Several experimental and theoretical bounds exist for the lambda parameters. Theory dictates that the λ_{ijk} are non-zero only if $i < j$, where the index denotes lepton or quark generation. In addition, all λ''_{ijk} parameters must be zero if LFV interactions are permitted for a theory to maintain a significant proton lifetime.

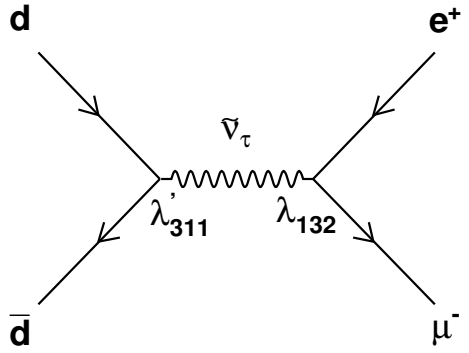

Figure 1: Feynman Diagram of RPV sneutrino production and decay. The diagram for Z'_0 is similar, with Q_u or Q_d substituted for λ'_{311} and Q^l_{12} for λ_{132}.

Consistent with these constraints, we assume in this analysis that all lambda parameters except λ_{132} and λ'_{311} are zero. These couplings govern the production of the tau sneutrino from $d\bar{d}$ and its decay into $e\mu$, as shown in the Feynman diagram of Figure 1. We do not consider decays to $e\tau$ and $\mu\tau$ that lead to a $e\mu$ final state here

but will address these modes in a future analysis. The current best limits for λ_{132} and λ'_{311}, 0.05 and 0.16, are provided by low energy experiments that measure deviations from SM predictions.[5]

In addition to testing the RPV sneutrino decay model, we also provide an interpretation of data in terms of the LFV decay of a neutral spin-1 particle. We consider an $E6$ theory that extends the SM by addition of an extra $U(1)$ gauge symmetry and a corresponding neutral gauge boson, the Z'_0 [6]. The coupling of the Z'_0 to $e\mu$ is given by a $U(1)'$ charge, Q^l_{12} that we constrain as a function of the Z'_0 mass.

We follow the conventions of a recent paper [1] citing the $E6$ model in order to facilitate a comparison with the results that paper presents. In plotting the next-to-leading order (NLO) $p\bar{p} \to Z'_0 \to e\mu$ cross section, we assume that the Z'_0 can decay to SM fermions only and that its couplings to right and left handed leptons are equal. The current best limits on Q^l_{12} and the Z'_0 mass follow from a search for muon conversion, $\mu \to eee$ and $\mu N \to eN$, by the SINDRUMII collaboration[7]. These limits are on order $10^{-8} \leq \frac{g_X^2}{g_Y^2} Q^l_{12} \leq 10^{-6}$ for Z'_0 masses in our search range.

2 Event Selection

2.1 Data Format & Pre-Selection Cuts

All datasets and Monte Carlo samples used in the analysis are formatted as cdfsoft version 5.3.3_nt5 TopNtuples. The ntuples are produced from the output of the inclusive lepton filter in TopFind module, which applies a loose subset of the full lepton ID cuts described below. The cuts in TopFind are fully efficient with respect to our event selection and allow us to obtain ntuples of manageable size.

2.2 Lepton ID

We identify electrons and muons through application of the Top/EWK lepton ID cuts, detailed in [8] and [9]. Summaries of the cuts are provided in Tables 1 and 2. We consider central electrons only. Muons may be either CMUP, CMX, CMU-only or CMP-only.

Lepton identification efficiency has been shown to differ in data and Monte Carlo. [8][9] To achieve consistency with data, we apply ID scale factors (ϵ_{ID}) to the acceptances calculated in Monte Carlo. The specific scale factors we use are given in Table 3.

2.3 Trigger Requirements

We utilize data from the high P_T lepton datasets, bhel0d and bhm0d, that are products of the CEM18 and CMUP18/CMX18 trigger paths. In data we require that events pass the CEM18 trigger and, if the muon used is CMUP or CMX, the muon trigger associated with the muon type. If the muon is CMU-only or CMP-only we simply require that the events pass the CEM18 trigger.

Quantity	**Requirement**
DefEmObject	true
Region	CEM
Conversion	false
Fiducial	true
E_T	$\geq$ 20 GeV
Track Axial Segments	≥ 2
Track Stereo Segments	≥ 2
Track P_T	$\geq$ 10 GeV
Hadem	$\leq (0.055 + (0.00045 \times Energy))$
E/P	$\leq 2.0 \parallel P_T \geq$ 50 GeV
$\mid TrackZ_0 \mid$	$\leq$ 60 cm
$\mid CES\Delta Z \mid$	$\leq$ 5 cm
Charge $\times\Delta X_{CES}$	-3 cm $\leq$, $\leq$ 1.5 cm
LshrTrk	≤ 0.2
Stripχ^2	≤ 10
Isolation	≤ 0.1

Table 1: Electron Identification Cuts. Tight Top/EWK electron ID cuts and their values.

Quantity	**Requirement**
DefMuonObject	true
P_T	$\geq$ 20 GeV
HadEnergy	$\leq max(6., 6. + 0.0280 \times (P - 100.))$
EmEnergy	$\leq max(2., 2. + 0.0115 \times (P - 100.))$
$\mid TrackZ_0 \mid$	$\leq$ 60 cm
Track Axial Segments	≥ 3
Track Stereo Segments	≥ 3
$\mid D_0 \mid$	$\leq$ 0.20 if TrackSiHits==0
	$\leq$ 0.02 if TrackSiHits > 0
Isolation	≤ 0.1
$\mid CmuDx \mid$	$\leq$ 3.0 if CMUP, CMU
$\mid CmpDx \mid$	$\leq$ 6.0 if CMUP, CMP
$\mid CmxDx \mid$	$\leq$ 6.0 if CMX
$\mid \rho(\eta, Z_0, 155) \mid$	$>$ 140 if CMX

Table 2: Muon Identification Cuts. Tight Top/EWK muon ID cuts and their values.

We emulate the effect of the trigger in Monte Carlo by applying trigger efficiencies[10][9]. For each $e\mu$ category we apply a factor, ϵ_{trig}, that is derived from the efficiencies and

Lepton Type	ϵ_{ID}
CEM	0.996
$CMUP$	0.930
CMX	1.002
CMU	0.923
CMP	0.950

Table 3: Lepton ID Scale Factors. These factors are used to scale the lepton ID efficiency of Top/EWK cuts in Monte Carlo to the corresponding values in data [8] [9].

represents the probability for an $e\mu$ event to pass the relevant triggers. For the CMU-only and CMP-only categories this factor is just the CEM trigger efficiency. The specific factors we use are listed in Table 4 below.

Electron type	Muon type	Trigger	ϵ_{trig}
CEM	CMUP	CEM18‖CMUP18	.9996
CEM	CMX	CEM18‖CMX18	.9998
CEM	CMU	CEM18	.9660
CEM	CMP	CEM18	.9660

Table 4: Trigger Efficiency Scale Factors. These factors represent the probability for a particular $e\mu$ category to pass the associated trigger(s). They are used to correct our Monte Carlo acceptances for the effect of the trigger selection in data.

2.4 Event-Level Cuts

We consider events with at least one electron and one muon that pass the lepton ID cuts described above. In addition, we require that the electron and muon have opposite charge and that the difference in their track Z_0 be less than 5 cm. In events containing several $e\mu$ combinations that pass our cuts we select the highest P_T pair. Events flagged as cosmics in the TopSummary object are rejected. No requirements are made of missing transverse energy or jets.

3 Signal Monte Carlo

We model the sneutrino signal in PYTHIA using the Higgs as a substitute, which we force to decay to $e\mu$ by altering the default PYTHIA decay table. We generate 10K

events at nine mass points between 50 and 800 GeV, perform simulation/production on the generated events and ntuple the reconstructed output. The software used for this procedure is provided in an archive of pre-built binaries from the Top Group. All modules in the archive are cdfsoft version 5.3.3_nt5. We apply the event selection criteria to the ntuples and count the number of passing events in each $e\mu$ category. This provides raw acceptances for the categories that we correct using ϵ_{tot}, the combination of ϵ_{ID} and ϵ_{trig} corresponding to the specific $e\mu$ category. We recombine the corrected acceptances to obtain an overall acceptance that we use in the calculation of observed signal cross section.

We follow a similar procedure in modeling the Z'_0 signal. We choose the Z'_0 resonance process in PYTHIA and force the Z'_0 to decay to $e\mu$. Pure V-A or V+A $Z'_0\bar{f}f$ couplings are favored in $E6$ models that include LFV and we specify left-handed couplings without loss of generality. The assumed $Z'_0\bar{f}f$ couplings influence the measured signal acceptance because they determine the angular distribution of the Z'_0 decay products. The angle made by the electron or muon in the Z'_0 rest frame with respect to the beam axis is conventionally termed θ^*. As shown on the left in Figure 2, our choice of pure left-handed couplings results in the $(1 - cos\theta^*)^2$ and $(1 + cos\theta^*)^2$ distributions expected for e^+ and e^-.

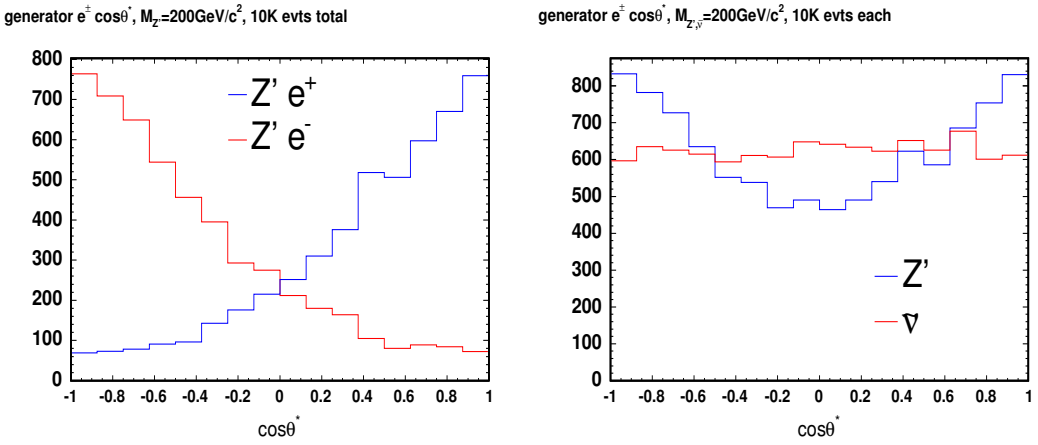

Figure 2: Angular Distributions. The angular distributions of electrons and positrons from Z'_0 decay in the Z'_0 rest frame are shown on the left. Their combined distribution, right, contrasts with that from isotropic $\tilde{\nu}_\tau$ decay. The excess of $cos\theta^* \approx 1$ leptons from Z'_0 decay leads to a smaller acceptance relative to the $\tilde{\nu}_\tau$.

We show the $cos\theta^*$ distribution of electrons and positrons from 200 GeV/c^2 Z'_0 and $\tilde{\nu}_\tau$ decays in the plot on the right in Figure 2. The distributions for muons are similar and are not shown. The relative difference in the number of electrons and muons with

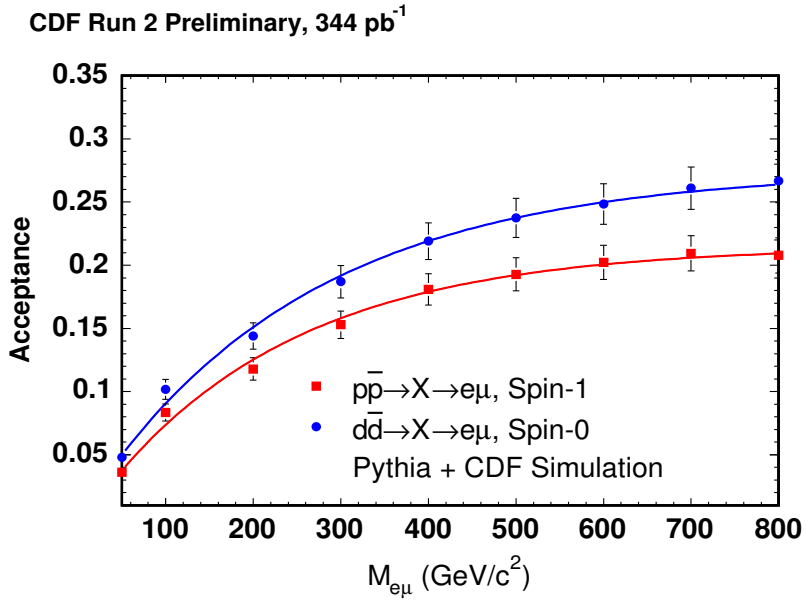

Figure 3: Signal Acceptance. Z'_0 acceptances are smaller than those for $\tilde{\nu}_\tau$ because of a relative difference in the angular distributions of the decay products.

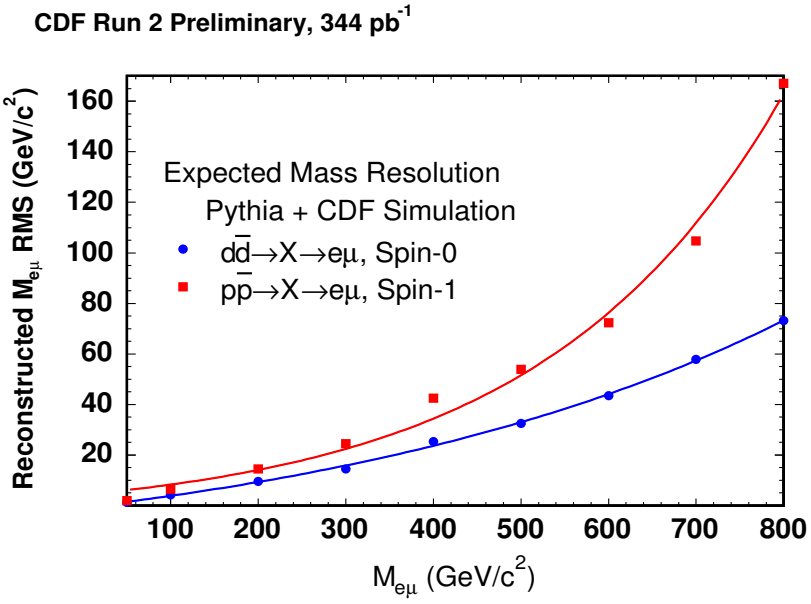

Figure 4: RMS. Fits to the RMS of the signal $M_{e\mu}$ distributions are used to set the width and location of the acceptance window in our sensitivity and observed cross section calculations.

$cos\theta^* \approx \pm 1$ shown in Figure 2 explains the difference in acceptance apparent in Figure 3. The Z_0' and $\tilde{\nu}_\tau$ are produced with large P_Z and leptons from Z_0' decay are less likely to be identified as central because they emerge preferentially in the z-direction.

While signal acceptance clearly factors in the calculation of the sneutrino cross section, we follow a procedure with an additional dependence on the width of the invariant $e\mu$ mass ($M_{e\mu}$) distributions. In Section 6.1 we describe a method in which an acceptance window of size 3σ is swept in mass by steps of $\sigma/10$. For the purpose of that discussion, we include $M_{e\mu}$ distributions from sneutrino decay in Appendix A. Figure 4 plots the RMS extracted from these and the corresponding Z_0' $M_{e\mu}$ distributions. The distributions broaden with increasing particle mass due to degradation in momentum resolution with increasing P_T.

4 Backgrounds

4.1 Physics Backgrounds

The important physics backgrounds in our search are the leptonic decays of $Z_0 \rightarrow \tau\tau$, $t\bar{t}$, and dibosons. The cross sections we use for $t\bar{t}$ and diboson production are their NNLO values, taken from the PDG. We obtain a NLO cross section for $Z_0 \rightarrow \tau\tau$ by applying a 1.42 K-factor [11] to the leading order cross section used in generation. The Drell-Yan sample is constructed from the output of a leptonic filter and the associated efficiency (.1365) is included in its calculated acceptance.

We correct acceptances for the SM backgrounds using the same method we apply to signal Monte Carlo; raw acceptances are calculated for each $e\mu$ category, corrected with ϵ_{tot} and recombined. We use the corrected acceptances, cross sections and luminosity of our data sample to calculate an expected number of background events for each SM channel. Figure 5 shows a stack of the background $M_{e\mu}$ distributions, each normalized to expectation.

4.2 Fake Lepton Backgrounds

Fake leptons are an additional source of background in our search. Jets that deposit a significant amount of their energy in the electromagnetic calorimeters may be reconstructed as electrons. These fake electrons, paired with real muons, may pass our event selection criteria and contribute to an $e\mu$ signal. Likewise, pions that "punch-through" to the muon chambers may be identified as isolated muons and, together with real electrons, enter our signal region. We estimate the background contribution from fake leptons by applying fake rates, determined from several jet-enriched data samples, to our high P_T lepton dataset.

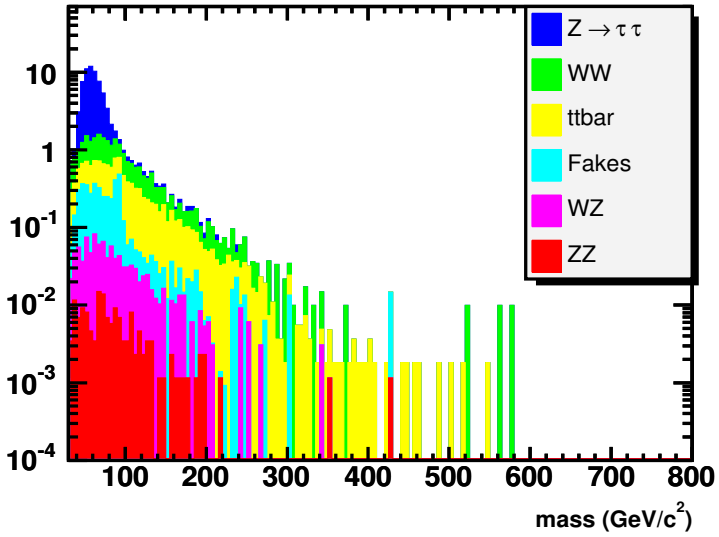

Figure 5: Background $M_{e\mu}$ Distributions. This plot shows stacked $M_{e\mu}$ distributions of the physics and fake backgrounds scaled to theoretical predictions. $Z \rightarrow \tau\tau$ is the largest source of background and contributes primarily at low (<100 GeV/c^2) $M_{e\mu}$.

4.2.1 Fake Probabilities

Our treatment of fake leptons is based on a technique developed by the Top-Dilepton ("DIL") Group [12]. We define fake rates as the probability for a "fakeable object", a loosely defined CdfEmObject or CdfMuon associated with a jet, to pass the full lepton identification criteria. We determine fake rates by dividing the number of fakeable objects that pass the ID cuts described in Section 2.2 by the total number of fakeable objects in a sample. The cuts defining the fakeable objects denominators are listed in Tables 5 and 6.

Quantity	Value
Region	CEM
Conversion	false
Hadem	$\leq (0.055 + (0.00045 \times En))$

Table 5: Denominator CdfEmObject Cuts. These cuts define the loosely identified CdfEmObjects appearing in the denominator of our CEM fake rate. They are a subset of the full electron ID cuts.

Quantity	Requirement
Fiducial	true
$\mid D_0 \mid$	≤ 0.20 if TrackSiHits==0
	≤ 0.02 if TrackSiHits > 0

Table 6: Denominator CdfMuon Cuts. These cuts define the CdfMuon objects appearing in the denominators of our muon fake rates. They are a subset of the full muon ID cuts.

We calculate fake rates in the Jet20, Jet50, Jet70 and Jet100 data samples. We remove trigger bias from the jet samples by selecting jets that do not exclusively satisfy the trigger criteria. In this approach, all jets in an event are considered unbiased if multiple jets in that event pass the trigger requirement. If only a single jet in an event passes the trigger, that jet is considered to be biased. In determining which jets pass the trigger it is necessary to recalculate jet E_T with the actual event Z_0 used in the Level 3 trigger, rather than using the default jet E_T values calculated with $Z_0 = 0$. Figure 19 in Appendix B shows the jet E_T before and after the unbiasing procedure.

We remove real leptons from the unbiased samples by rejecting events in which the invariant mass of a denominator object pair falls between 76 and 106 GeV/c^2 (to remove Z_0's) or in which the transverse mass formed from the missing E_T and denominator object is greater than 50 GeV/c^2 (to remove W's). These requirements reject an average of 1% and 10% of events from the samples. Finally, we count the number of objects passing the numerator and denominator cuts and form the fake ratios, shown in the plots of Appendix B. The electron and muon fake rates show a dependency on E_T and P_T respectively and we therefore parameterize in terms of these quantities. We combine results from the CMUP and CMX categories (labeled TMUO in the figure) and the CMU-only and CMP-only categories (LMUO) to improve statistics.

The weighted average of results from each sample is indicated with black squares in the plots of Figure 20. We use this parameterized average to estimate the background contribution from fakes leptons in the high P_T lepton samples. We select events containing one lepton passing the ID cuts of Section 2.2 and at least one fakeable objects of alternate flavor. We reject an event if it contains electrons *and* muons that pass the identification cuts. We then impose the event-level cuts and trigger requirements to all combinations of real + fakeable objects in the event. Those passing are binned in invariant mass and the relevant fake rate is applied. This provides the estimate of the background due to fake leptons as a function of $M_{e\mu}$ shown previously in Figure 5. The integrated number of expected fake events for the CEM, TMUO and LMUO categories are 2.34 ± 0.15, 0.34 ± 0.21 and 1.45 ± 0.79 .

5 Control Regions

5.1 $Z_0 \rightarrow ee$

We compare the $Z_0 \rightarrow ee$ invariant mass and cross section found from data and Monte Carlo samples to gain confidence in our ability to identify electrons. We use the ztop2i PYTHIA Monte Carlo ntuples (1M events) and the tight inclusive electron sample, bhel0d, for this study. The dataset represents 369.6 pb^{-1} after applying the DQM electron goodrun list v7 (no silicon) and a 1.019% luminosity correction[13]. Z_0's are selected from events containing at least two CEM electrons passing the electron identification cuts. Of these we require a pair that passes the event-level ΔZ_0^{trk} and opposite charge cuts with an invariant mass within 15 GeV/c^2 of the Z_0 mass.

Figure 6 compares the invariant mass distributions measured in data and Monte Carlo samples. Plots of the P_T of the higher and lower P_T electrons in the pair are shown in Appendix C. The relative shift between the data and Monte Carlo mass distributions has been observed in other analyses and is attributed to differences in the electron energy scale. We choose not to correct electron energy as a shift of this magnitude does not significantly impact our acceptance.

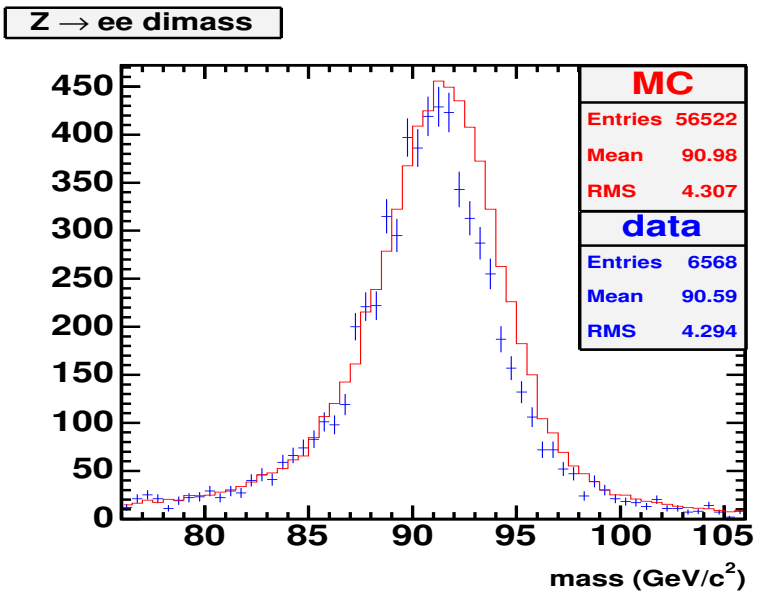

Figure 6: $Z \rightarrow ee$ **invariant mass.** Data (points) and Monte Carlo (line). The relative shift between data and Monte Carlo is due to a discrepancy in the electron energy scale. We do not correct for this as it will not significantly effect our acceptance.

We calculate an acceptance in the ztop2i sample after placing a 66 GeV/$c^2 \leq m_{ee} \leq$ 116 GeV/c^2 on the generator-level Z_0 mass to limit off-shell contributions. Doing so

permits comparison with the familiar leading order cross section of 252 pb. The acceptance (α) we determine in Monte Carlo is corrected using the ϵ_{tot} appropriate for two CEM electrons. Table 7 summarizes our results. We find good agreement between the measured and LO cross section given that we do not account for background contamination in data.

N_{data}	6568
luminosity	369.6 pb^{-1}
$\alpha \times \epsilon_{tot}$	6.28 ± 0.03 %
$\sigma \times BR$	260.5 ± 1.1 pb

Table 7: $Z \to ee$ **Cross Section Results.** Our measured cross section is consistent with the LO value of 252 pb. The difference observed is attributed to background contamination, which we do not subtract.

5.2 $Z_0 \to \mu\mu$

The procedure used in the $Z_0 \to \mu\mu$ control region is similar to that described above. We choose events with at least two identified muons and require a pair that passes our event-level and invariant mass cuts. We further stipulate that at least one of the muons be CMUP or CMX to satisfy the trigger requirements met in data. We use the bhm0d data sample representing 357.0 pb^{-1} after the DQM muon goodrun list v7 (no silicon) and a 1.019% luminosity correction is applied. The Monte Carlo sample, ztop0i, contains 2M events. Figure 7 compares the invariant mass distributions found in these dataset. [1]

The method we use to calculate the $Z \to \mu\mu$ cross section is again similar to that used for $Z \to ee$. In this case, however, we must apply separate corrections to the acceptances for each of the allowed muon combinations (*i.e.*:CMUP or CMX + CMUP,CMU,CMP, or CMX). The corrected acceptances from each category are recombined and the total corrected acceptance is used to calculate a cross section for data. Table 8 lists our results. The values are consistent considering that, again, we do not correct for background contamination.

5.3 30 GeV $\leq$ M$_{e\mu}$ $\leq$ 100 GeV

A low-mass $e\mu$ control region allows us to test our $e\mu$ event selection and the accuracy of our Monte Carlo background predictions. We apply the full event selection described in Section 2 with an added constraint of 30 GeV/c^2 $\leq M_{e\mu} \leq$ 100 GeV/c^2. This $M_{e\mu}$

[1] Gaussian smearing has been applied to the momentum in Monte Carlo

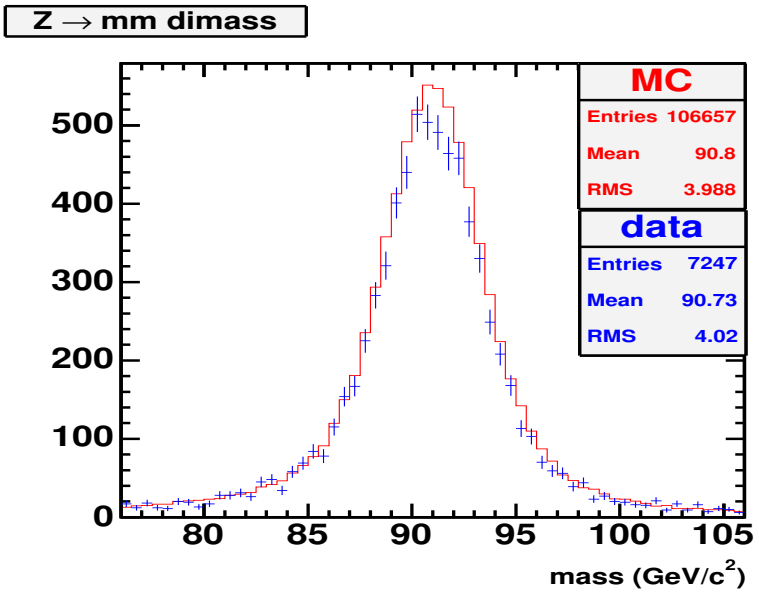

Figure 7: $Z_0 \to \mu\mu$ **invariant mass.** We find good agreement between data (points) and Monte Carlo (line). The distribution shown for Monte Carlo is constructed using the Gaussian smeared muon momenta and energy.

N_{data}	7247
luminosity	357.0 pb^{-1}
$\alpha \times \epsilon_{tot}$	7.96 ± 0.03 %
$\sigma \times BR$	255.2 ± 0.9 pb

Table 8: $Z_0 \to \mu\mu$ **Cross Section.** Our measured cross section is very close to the LO value of 252 pb even though do remove backgrounds.

region was excluded by the Run I analysis and allows us to test our procedure without bias.

As in the full analysis, we choose runs in data from marked "good" for both electrons and muons according to the v7 goodrun lists. This leaves us a dataset of 344pb^{-1} after applying the 1.019% luminosity correction. We additionally require that data events have trigger bits set for the CEM18 trigger and for the CMUP18 or CMX18 triggers if the muon is of corresponding type. We recalculate acceptances for the Monte Carlo samples in the 30-100 GeV/c^2 window and use their corrected values to predict an expected number of background events in each channel.

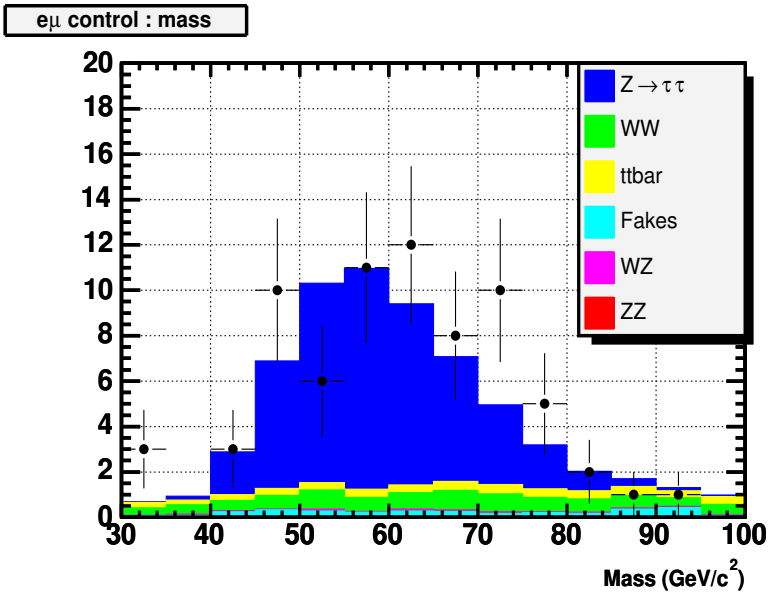

Figure 8: $e\mu$ **Control Region Mass Distributions.** Discounting fluctuations in data for several of the mass bins, the Monte Carlo and data distributions are consistent for the $e\mu$ control region.

Channel	Control Region	Signal Region
$Z \rightarrow \tau\tau$	$38.8 \pm 0.6 \pm 2.3$	$0.6 \pm 0.0 \pm 0.0$
diboson	$6.6 \pm 0.2 \pm 0.4$	$3.5 \pm 0.1 \pm 0.2$
$t\bar{t}$	$3.6 \pm 0.1 \pm 0.2$	$3.2 \pm 0.1 \pm 0.2$
fake lepton	$2.9 \pm 1.1 \pm 1.3$	$0.4 \pm 0.4 \pm 0.4$
Prediction	$51.9 \pm 1.1 \pm 2.7$	$7.7 \pm 0.4 \pm 0.5$
Observation	56	5

Table 9: $e\mu$ **Control and Signal Region Background Expectations.** We use corrected acceptances and theory cross sections to calculate the SM expectations for the high and low $M_{e\mu}$ regions. The total background expectations in both regions agrees with our observations.

6 Analysis

6.1 Sensitivity

Having obtained consistent results in the $e\mu$ control region, we assess our sensitivity to a RPV sneutrino signal and estimate a limit on its mass. Signal acceptance is taken from the fit shown in Figure 3 and, beginning with a 50 GeV/c^2 mass point, we step in mass to successive points using one tenth the RMS taken from the fit in Figure 4. We use the acceptance, number of observed and number of expected background events in a 3σ window around each mass point to calculate an upper limit on the sneutrino cross section. In calculating sensitivity we assume that in each mass window the number of observed events equals the background expectation. This assumption allows us to predict, in the absence of discovery, the limit we will set on the sneutrino mass.

We account for possible fluctuations in the backgrounds from their expected contributions by conducting a number of pseudo-experiments. We perform a series of trials in which the integrals of the background $M_{e\mu}$ distributions are Poisson fluctuated from their expectations. In each trial we sweep a 3σ mass window from 50-800 GeV in steps of $\sigma/10$ as described above and input the signal acceptance and background counts in the window to a Bayesian cross section calculator [14]. We also input the uncertainties on the background expectations and signal acceptance presented in Section 7. The Bayesian routine returns the number of expected signal events in the presence of background at the 95% C.L.

Equation 1 represents the LO cross section $\times$ branching ratio for $p\bar{p} \rightarrow \tilde{\nu}_\tau \rightarrow e\mu$ in the narrow width approximation [15]. In the scenario we consider, the Γ_i and Γ_f are proportional to the sneutrino mass $\times$ $(\lambda'_{311})^2$ and $(\lambda_{132})^2$. We begin with the current best limits for λ'_{311} and λ_{132}, 0.16 and 0.05 respectively, and input $\hat{s} = (1.96\text{TeV})^2$ and $\tau = m_{\tilde{\nu}_\tau}/s^2$. We obtain values for the cross section by performing a numeric integration of the parton distribution function at 558 mass points between 50-800 GeV/c^2 . The parton number densities for d and $\bar{d}$ are taken from the CTEQ6L library and software from the GSL [16] is used to integrate the density function. We assume a 100% sneutrino branching ratio to $e\mu$. We scale the LO cross section to NLO using K-factors given by [2].

$$\sigma(d\bar{d} \rightarrow \tilde{\nu}_\tau \rightarrow f) = \frac{4\pi^2}{9}\frac{\Gamma_{d\bar{d}}\Gamma_f}{m\hat{s}\Gamma_t} \times \int_\tau^1 dx \left[\bar{d(x)}d(\bar{\tau/x}) + d(x)d(\tau/x)\right]/x \quad (1)$$

$$\Gamma_i = \frac{3}{4} \times \frac{\lambda_i^2}{4\pi} m_{\tilde{\nu}_\tau} \quad \lambda_i = \lambda_{132}, \lambda\text{`}_{311} \quad \Gamma_t = \Gamma_{d\bar{d}} + \Gamma_f \quad (2)$$

We plot the average 95% C.L. observed cross section together with the numerically integrated LO cross section in Figure 9. We indicate 1 and 2 σ error bands on the average. The intersection of the theory curve with the expected observation in the plot suggests that we may expect to set a limit near 430 GeV/c^2.

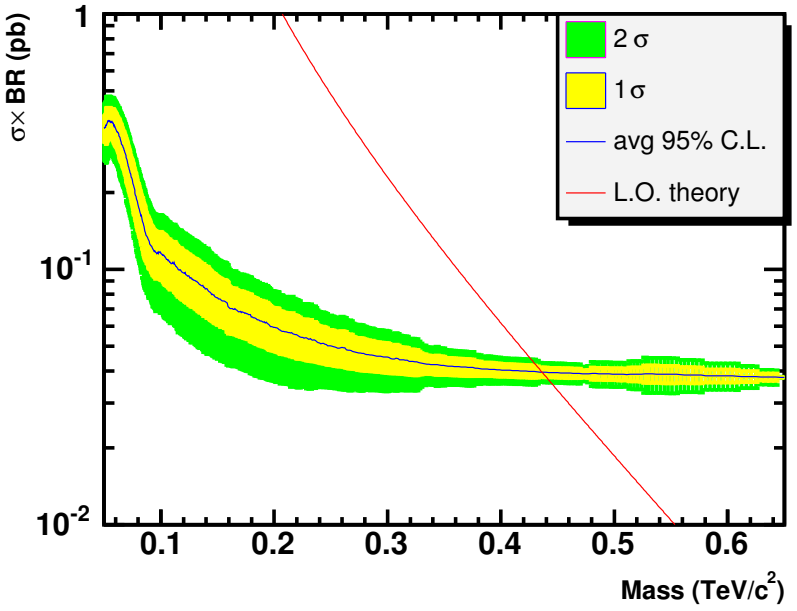

Figure 9: Sensitivity. The leading order cross section times branching ratio (red) is shown with the average 95% C.L SM prediction. The intersection of the theory curve with our sensitivity bands suggests a limit near 430 GeV/c^2.

Figure 10 compares the average 95% C.L. sensitivity, shown in blue, with results from a particular pseudo-experiment that assumes SM + sneutrino contributions. For this scenario we calculate an expected number of signal events for a 300 GeV/c^2 sneutrino using the LO cross section and acceptance at that mass value. The result, 16.2 events, is Poisson fluctuated and then used to select a total number of events from the signal $M_{e\mu}$ distribution shown in Appendix A. These events are added to the SM prediction to yield a combined SM+sneutrino prediction, shown in black. The sneutrino peak is broad due to the sliding acceptance window we use in calculating sensitivity.

We do not perform a sensitivity study for the Z_0' since this interpretation was added after the full sneutrino analysis was complete. We use the LO $p\bar{p} \to Z_0' \to e\mu$ cross section provided by [6] in what follows and scale to NLO using a 1.3 K-factor.

6.2 SM Consistency

Data and Monte Carlo $M_{e\mu}$ distributions are shown together in Figure 11 and their agreement indicates the consistency of our results with the SM. We attempt to quantify the level of agreement by performing a χ^2 test. Before unblinding our signal region we chose a variable width binning scheme designed to equalize Monte Carlo bin occupancies to roughly 5 events. This occupancy is selected to satisfy the Gaussian

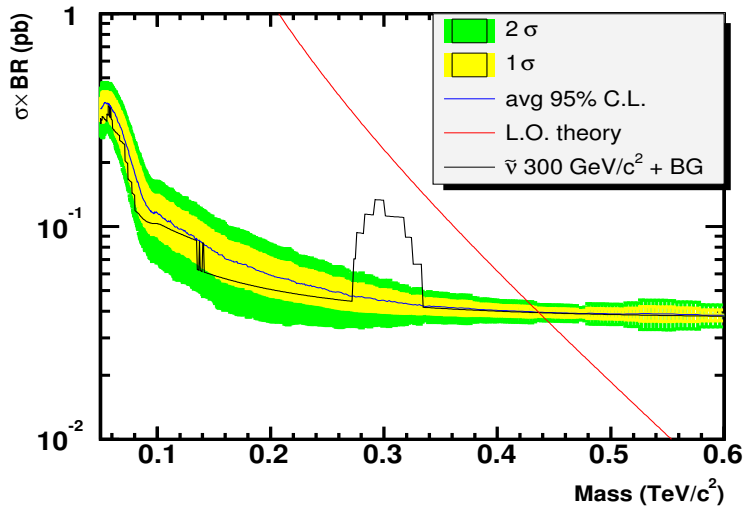

Figure 10: Cross Section for $\tilde{\nu}$ hypothesis. Average sensitivity (blue) is shown with results of particular a pseudo-experiment (black) that assumes a 300 GeV/c^2 sneutrino signal. The peak near 300 GeV/c^2 shows that we are sensitive to leading order predictions.

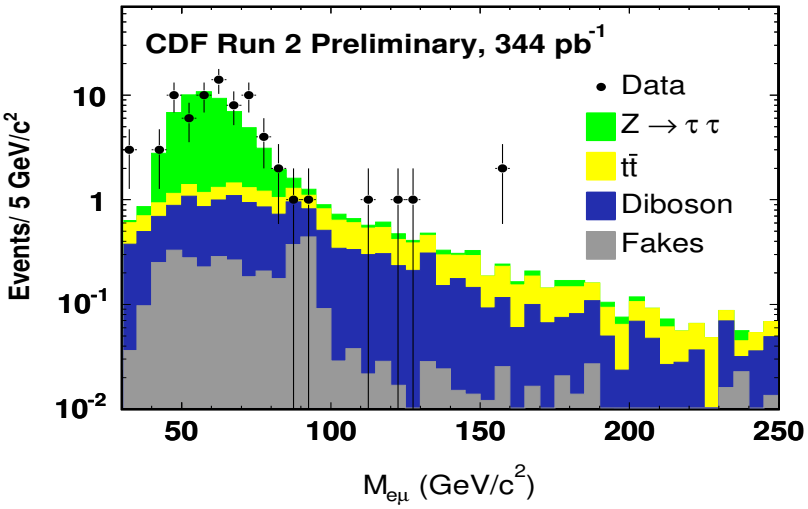

Figure 11: Data vs. Monte Carlo $M_{e\mu}$ Distributions. The combined Monte Carlo $M_{e\mu}$ distributions are plotted against data and their agreement suggests consistency with the SM.

approximation of the Poisson distributed data that is assumed in the χ^2 test. We are left with 14 bins, with the lower edge of the upper-most bin placed at 114 GeV. Table 11 in Appendix F provides the upper edge, observation and SM prediction for each bin. We also provide the reduced χ^2 statistic for the distribution and the associated p-value appropriate for 14 bins. The determined p-value is larger than 0.05 and we can therefore retain the SM hypothesis at this significance level.

6.3 Limits

Figure 12 shows the results of the Bayesian cross section calculations applied to data. These are overlaid on the sensitivity and theory curves shown previously. The plots demonstrate good agreement between the upper limit $p\bar{p} \to \tilde{\nu}_\tau \to e\mu$ and $p\bar{p} \to Z'_0 \to e\mu$ cross sections determined in data and our predicted sensitivity. The small peak near 150 GeV/c^2 contains 2 events and its squarish shape coincides with these events falling into and out of the sliding acceptance window used in the cross section calculation. The observed cross section for the $\tilde{\nu}_\tau$ hypothesis lies lower than that for Z'_0 due to the larger $\tilde{\nu}_\tau \to e\mu$ acceptance.

We conclude that our data does not contain evidence of $\tilde{\nu} \to e\mu$ or $Z'_0 \to e\mu$ decays and set limits on the $\tilde{\nu}_\tau$ and Z'_0 masses and couplings. Excluded masses are determined from the intersection of the observed and NLO cross section curves and depend, therefore, on the particular values assumed for the $e\mu$ couplings. The $\tilde{\nu}_\tau$ NLO cross section drawn in Figure 12, for example, is calculated using the current best limits of λ_{132} and λ'_{311}, 0.05 and 0.16. We independently vary λ_{132} and λ'_{311} from their current limits and plot the range of $M_{e\mu}$ values at which the observed and predicted cross sections intersect. Results from this procedure are shown in Figure 13. These plots depict excluded regions for $M_{e\mu} - \lambda_{132}$ and $M_{e\mu} - \lambda'_{311}$ given various values of the alternate coupling.

We construct the excluded $M_{e\mu} - Q^l_{12}$ regions shown in Figure 14 using NLO cross sections from four popular $E6$ models. The limits shown in Figure 14 are illustrative only since none of the models admit LFV Z'_0 decays. It is useful however to constrain the Q^l_{12} LFV coupling in the context of these models since together they are representative of general $E6$ theories. Figure 15 presents our Z'_0 results in an additional context. As described in [17], model-dependence in the $p\bar{p} \to Z'_0 \to l^+l^-$ cross section may be ascribed to two parameters, c_u and c_d. Our limits on the observed Z'_0 cross section translate directly to excluded regions in the $c_u - c_d$ plane.

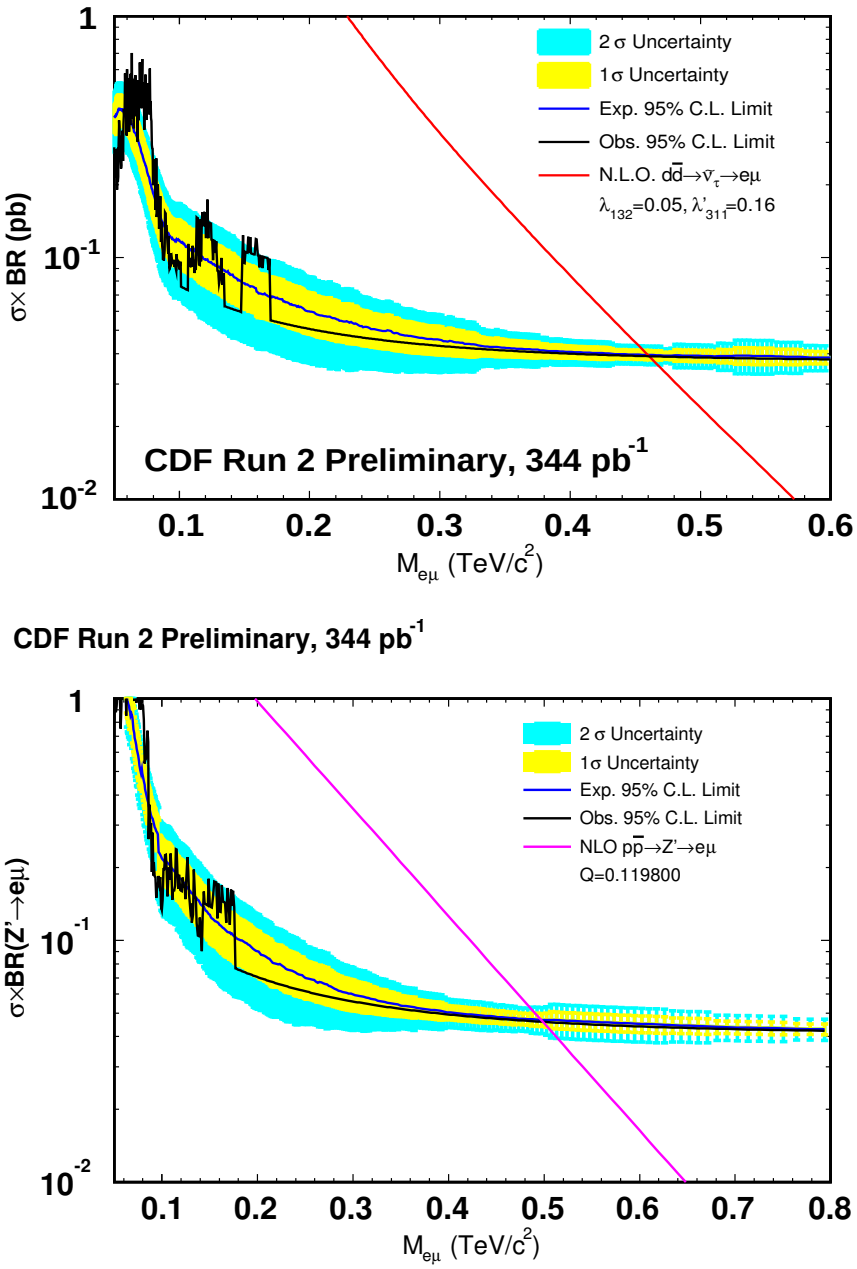

Figure 12: Observed Signal Cross Sections. Cross sections calculated from data are shown with NLO curves that assume the indicated values for the $e\mu$ couplings. The small peaks in data are consistent with fluctuations from our background predictions. We find no evidence for RPV sneutrino decay.

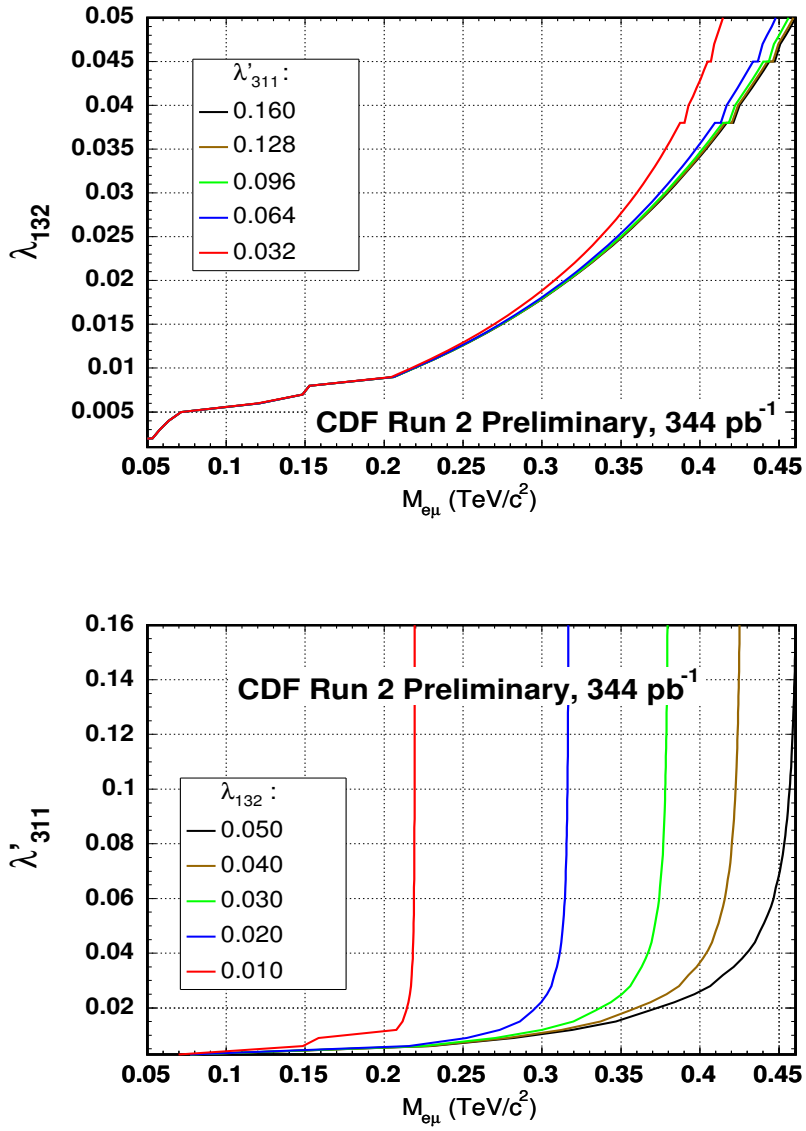

Figure 13: $M_{e\mu} - \lambda_{132}(\lambda'_{311})$ **Exclusion Regions.** These curves indicate excluded values for $\lambda_{132}(\lambda'_{311})$ as a function of $\tilde{\nu}_\tau$ mass and $\lambda'_{311}(\lambda_{132})$.

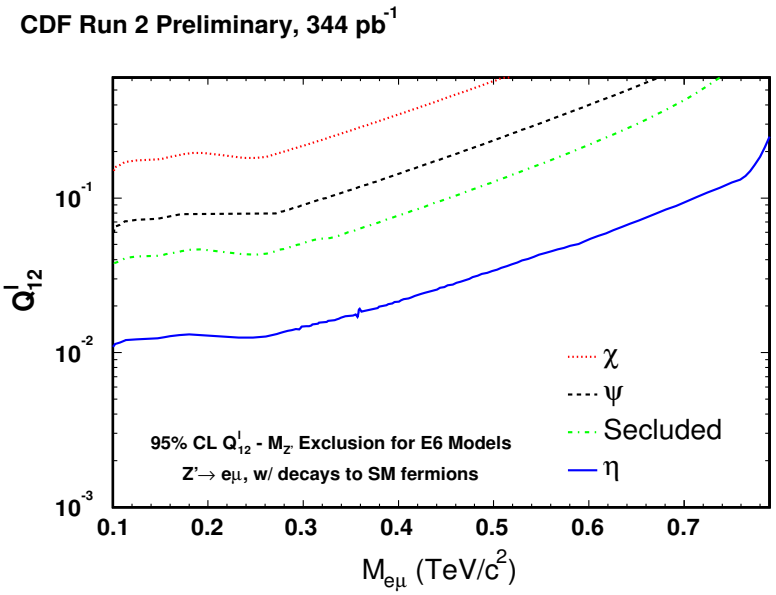

Figure 14: $M_{e\mu} - Q^l_{12}$ **Exclusion Region.** Regions above the curves represent excluded values for Q^l_{12} as a function of Z'_0 mass. The displayed limits are meant as an illustration of our experimental reach as none of the $E6$ models contain a LFV coupling. The value of the Z'_0 coupling at the production vertex is fixed by the particular models.

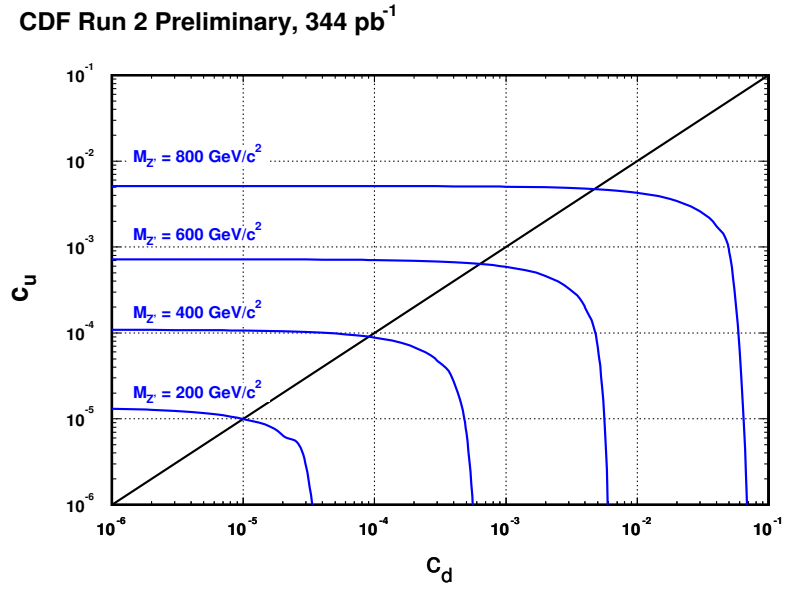

Figure 15: $c_u - c_d$ **Exclusion Region.** Regions above the curves indicate excluded combinations of the model-dependent c_u and c_d parameters.

6.4 Godparenting Update

Following a suggestion of our Godparents, we now use a slightly different technique in our calculation of the upper limit cross sections. Instead of imposing somewhat arbitrary 3σ acceptance windows on the $e\mu$ invariant mass spectrum, we now weight all data and background in the 100 to 800 GeV/c^2 range by values determined from the $e\mu$ mass resolution measured in our signal Monte Carlo samples. We replace the acceptance window with a unit normalized Gaussian distribution of mass-dependent width. We step across the mass range in units of 10 GeV/c^2 and use this distribution to assign weights to all data and background at each step. The weighted data and background event totals are input to the Bayesian upper limit calculation, described in section 6.1. This technique allows us to smooth the structure apparent in Figure 12 and does not significantly change the λ,λ' and Q^l_{12} exclusion regions in Figures 13 and 14. Figure 16, below, shows the result of this technique for the upper limit $d\bar{d} \rightarrow \tilde{\nu}_\tau \rightarrow e\mu$ cross section.

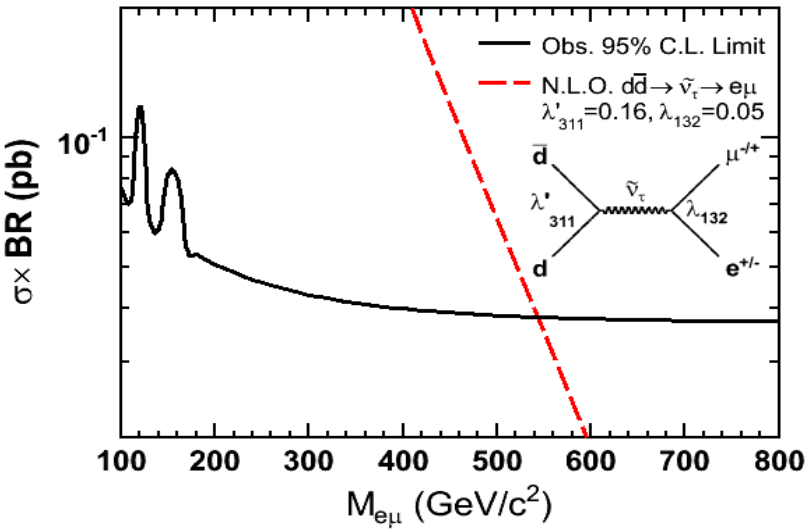

Figure 16: Upper Limit and NLO $\sigma \times BR$ This plot shows the upper limit NLO $\sigma \times BR$ calculated with the new weighting technique.

Figure 17 shows the new $\lambda'_{311} - M_{e\mu}$ and $Q^l_{12} - M_{e\mu}$ limits calculated from the smoothed upper limit cross sections. Kinks in the limits shown in Figures 13 and 14 coincide with spikes in the upper limit cross sections. These kinks are softened in Figure 17 due to the continuous upper limit cross sections obtained with the new method.

We now construct λ_{132} and λ'_{311} exclusion regions using new values for the $d\bar{d} \rightarrow \tilde{\nu} \rightarrow e\mu$ cross section times branching ratio. We use NLO $d\bar{d} \rightarrow \tilde{\nu}$ production cross

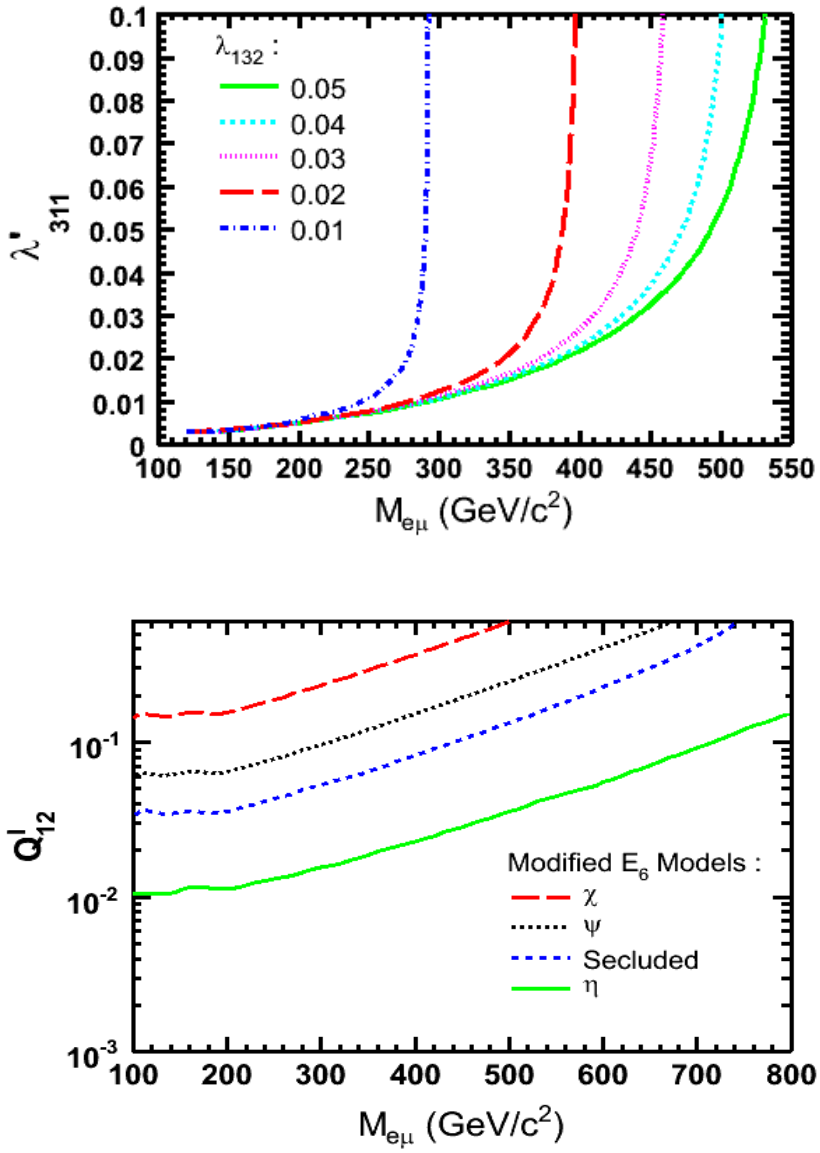

Figure 17: λ'_{311} and Q^l_{12} - $M_{e\mu}$ Exclusion Regions. These plots show the exclusion regions constructed using smoothed upper limit cross sections.

sections provided by the authors of [2], since these are consistently used in other CDF analyses that involve resonant sneutrino production. The authors provided us with a list of NLO $\tilde{\nu}_i$ production cross section values for $\lambda'_{i11} = 0.1$ as a function of $\tilde{\nu}_i$ mass. We scale these values to the specific λ'_{311} values used in the construction of the exclusion regions and multiply with a branching ratio of the form shown in Equation 1, *ie:* $\frac{(\lambda_{132})^2}{(\lambda'_{311})^2+(\lambda_{132})^2}$.

7 Systematic Uncertainties

Systematic uncertainties on signal acceptance and background estimates have an impact on the limits we set. Table 10 lists estimates for the uncertainties we've addressed. The remainder of this section discusses how these estimates are obtained.

$\alpha_t \times L$ Uncertainty Source	Fractional Sys. Uncert.
E & P Resolution	3.2%
PDF's	2.4%
Scale Factors	1.6%
Luminosity	6%
N_{BG} Uncertainty Source	Fractional Sys. Uncert.
Luminosity	5.6%
Fake Probabilities	3.1%

Table 10: Systematic Uncertainties. Values for the uncertainties that effect signal acceptance and background estimates.

- *Signal acceptance.* Uncertainties in the widths of the simulated signal $M_{e\mu}$ distributions are related to uncertainties in energy and momentum resolution and will influence the size of the 3σ mass window used in the limit calculation. In order to understand this relationship, we first smear the generator level energy and momenta with resolution functions in order to match the reconstructed distributions. We then vary the resolution by its uncertainty and determine the effect on acceptance. The momentum and energy resolution functions we use are given in [18] and [19]. The parametrization of momentum resolution contains a term with a factor of $(.15 \pm .02\%)$ however we find that significantly smaller values (0.0075% for electrons and 0.05% for muons) are required for agreement between the smeared and reconstructed distributions. We vary the resolutions by the scaled .02% momentum resolution uncertainty (6% for energy) and find a 3.2% relative acceptance difference.

- *PDF's.* Uncertainties due to PDF's are estimated using a technique described in [20]. In this approach, one weights the acceptance calculated using CTEQ5L PDF's with a set of scale factors to determine corresponding acceptances for alternate PDF's. We apply 40 different scale factors to determine the variation in acceptance due to uncertainties in the 20 eigenvectors of the CTEQ6M PDF set. Adding the percent acceptance differences in quadrature we find a 2.4% as the relative uncertainty due to PDF's..

- *Luminosity.* A 6% uncertainty is quoted on luminosity[13].

- *Lepton ID Cuts.* A 0.1% systematic is quoted for the CEM electron ID scale factor[8]. Uncertainties of 0.51%, 0.56%, 0.94% and 0.84% are given for CMUP, CMX, CMU-only and CMP-only muons [9].

- *Fake Rates.* Uncertainties in the expected number of fake leptons are measured from the cross-sample differences in fake rates. Their uncertainty introduces a 3.1% relative uncertainty on the expected background.

8 Conclusion

We find no evidence for RPV $\tilde{\nu}_\tau$ or LFV Z'_0 decays to $e\mu$ in current Run II data. We therefore exclude a range of values for the RPV couplings λ_{132} and λ'_{311} as a function of $\tilde{\nu}_\tau$ mass. We additionally exclude values of the LFV $U'(1)$ charge Q^l_{12} and combinations of the model-dependent c_u and c_d parameters as functions of Z'_0 mass. We plan to extend this analysis by incorporating $e\tau$ and $\mu\tau$ decay modes in the near future. By incorporating the tau channels we hope to increase our sensitivity and explore limits on additional RPV and LFV couplings.

A Signal $M_{e\mu}$ Distributions

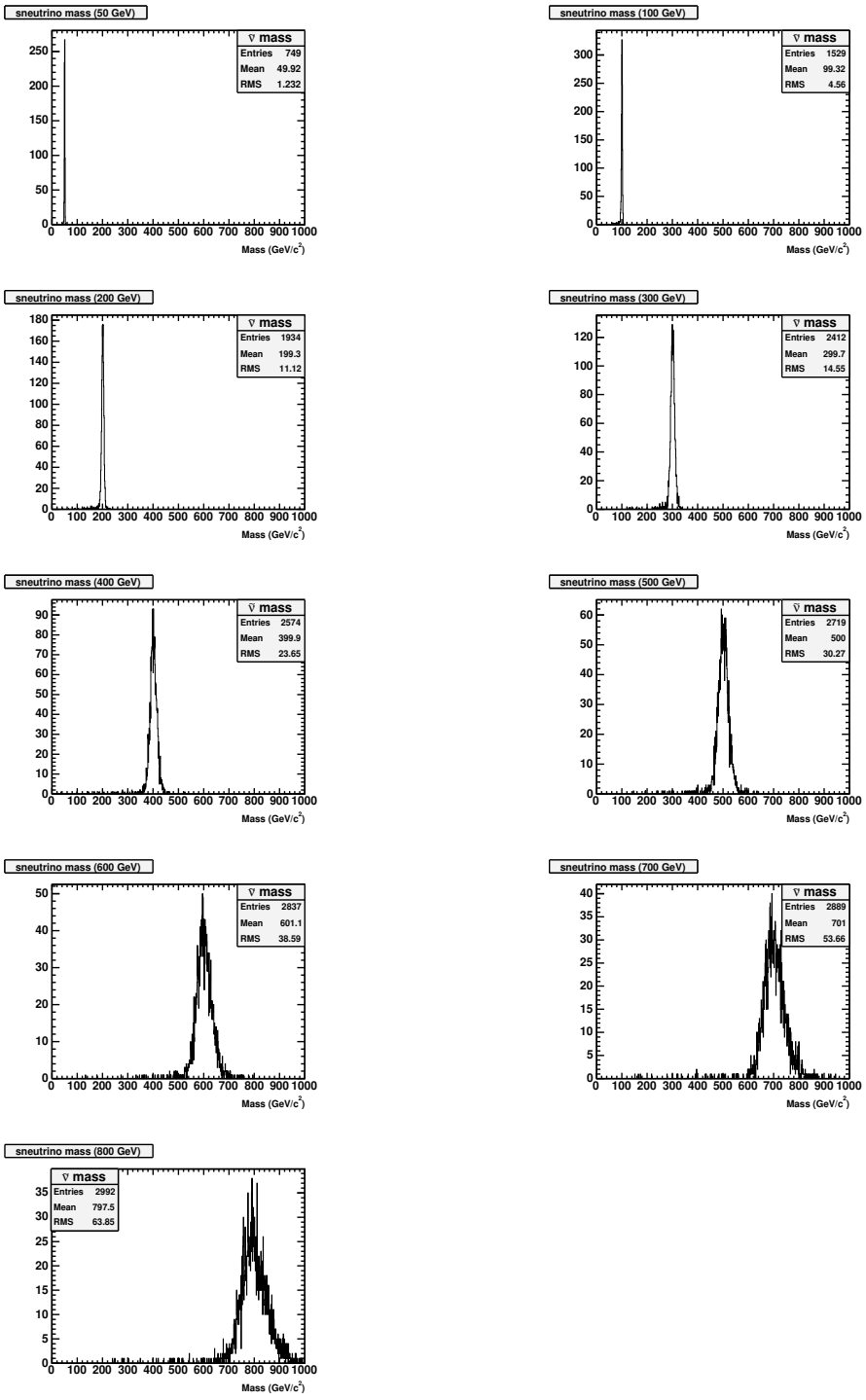

Figure 18: Signal Mass Distributions.

B Fake Rates

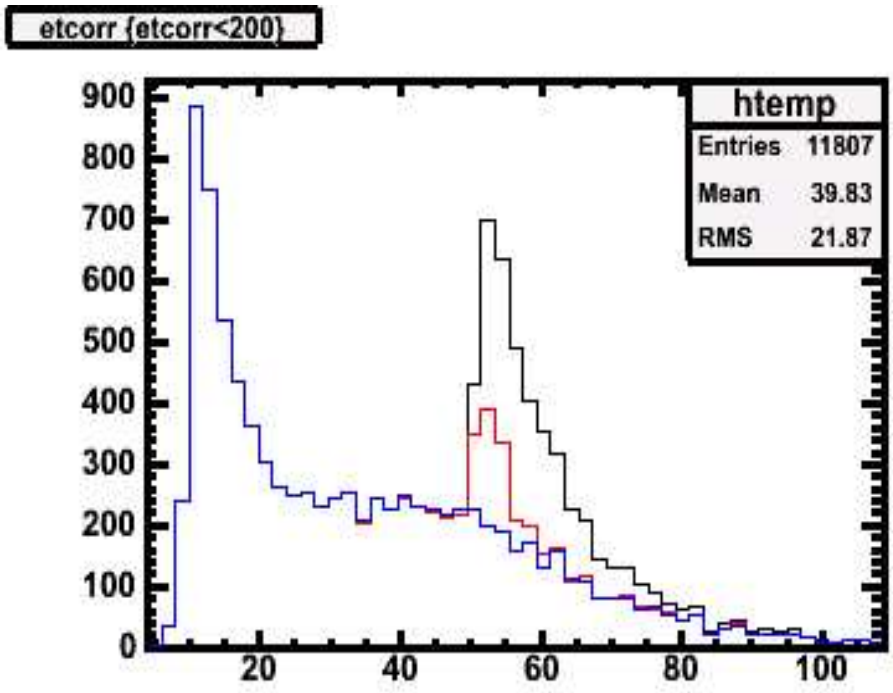

Figure 19: Jet Sample Unbiasing. This plot shows the raw E_T distribution from the Jet50 sample. The smaller peak at 50 GeV results when we apply our unbiasing procedure without first correcting the Jet E_T for the difference in on line vs. offline Z_0. The blue curve shows the distribution when we first apply this correction and indicates that we are able to remove most of the trigger bias.

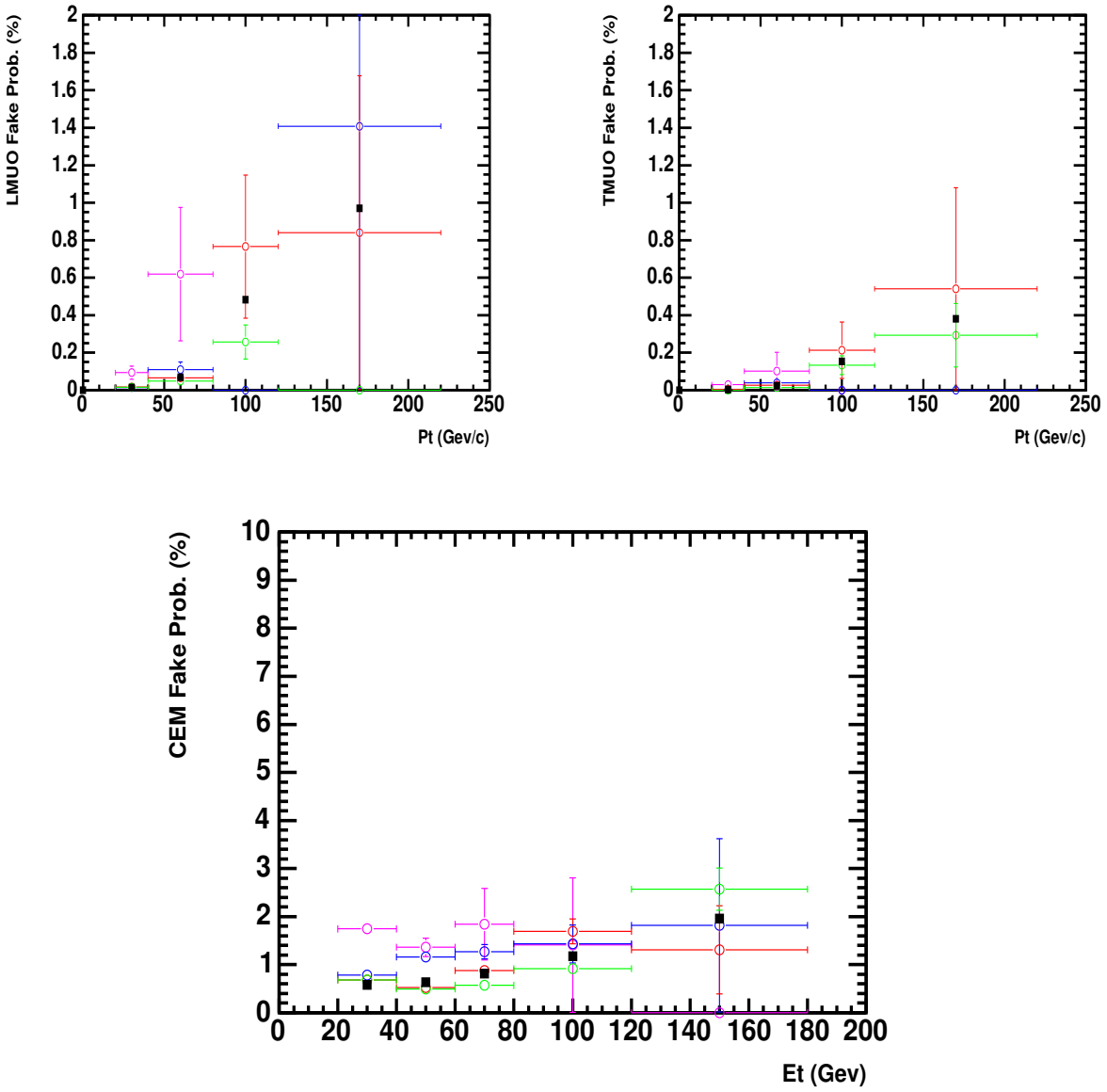

Figure 20: Fake rates. Fake rates for the different jet samples are shown above. Magenta=jet20, blue=jet50, red=jet70, green=jet100. The measured fake rates are generally consistent and differences between the samples will be used to estimate the uncertainty on our fake lepton background.

C $Z \to ee\ P_T$

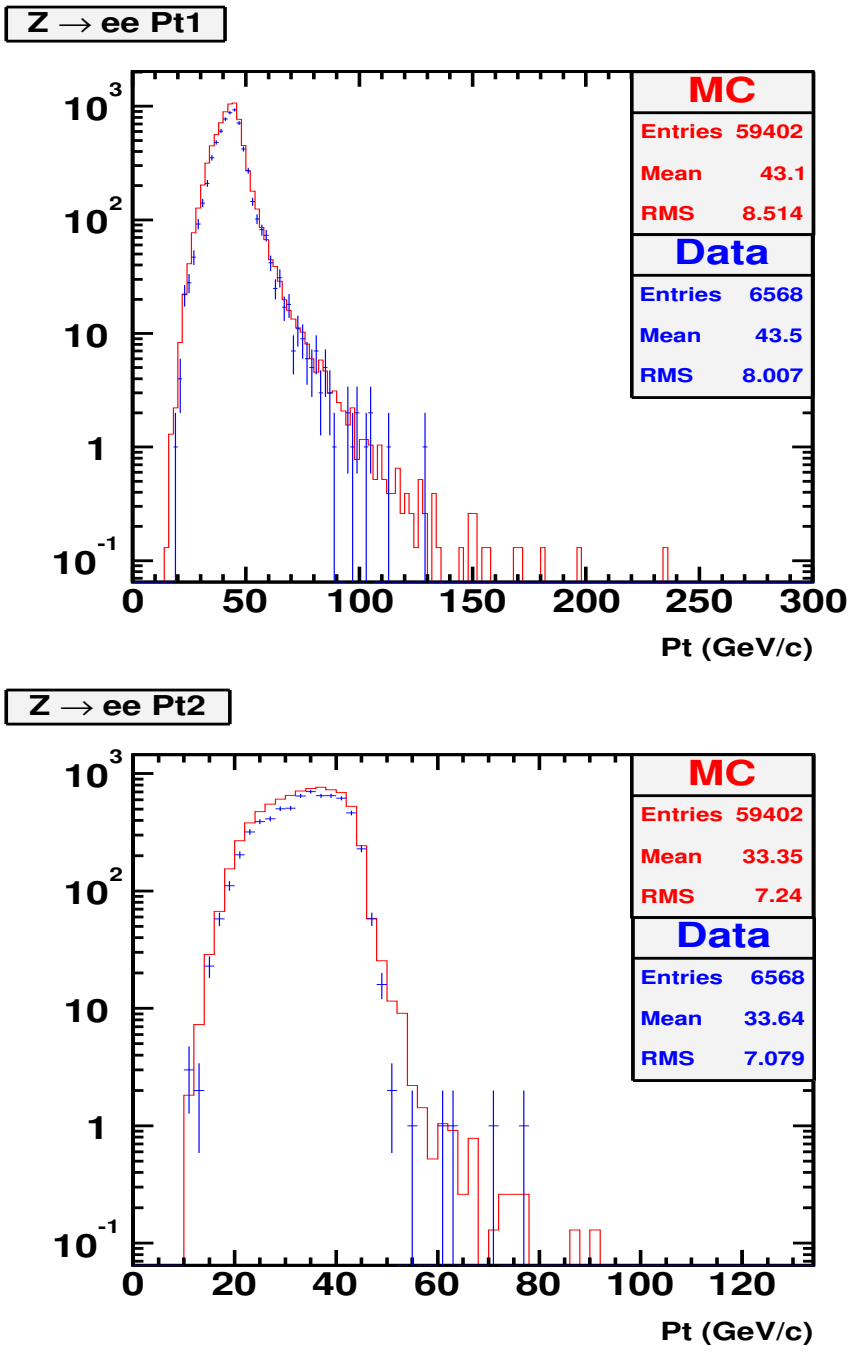

Figure 21: $Z \to ee\ P_T$.

D $Z \rightarrow \mu\mu$ P_T

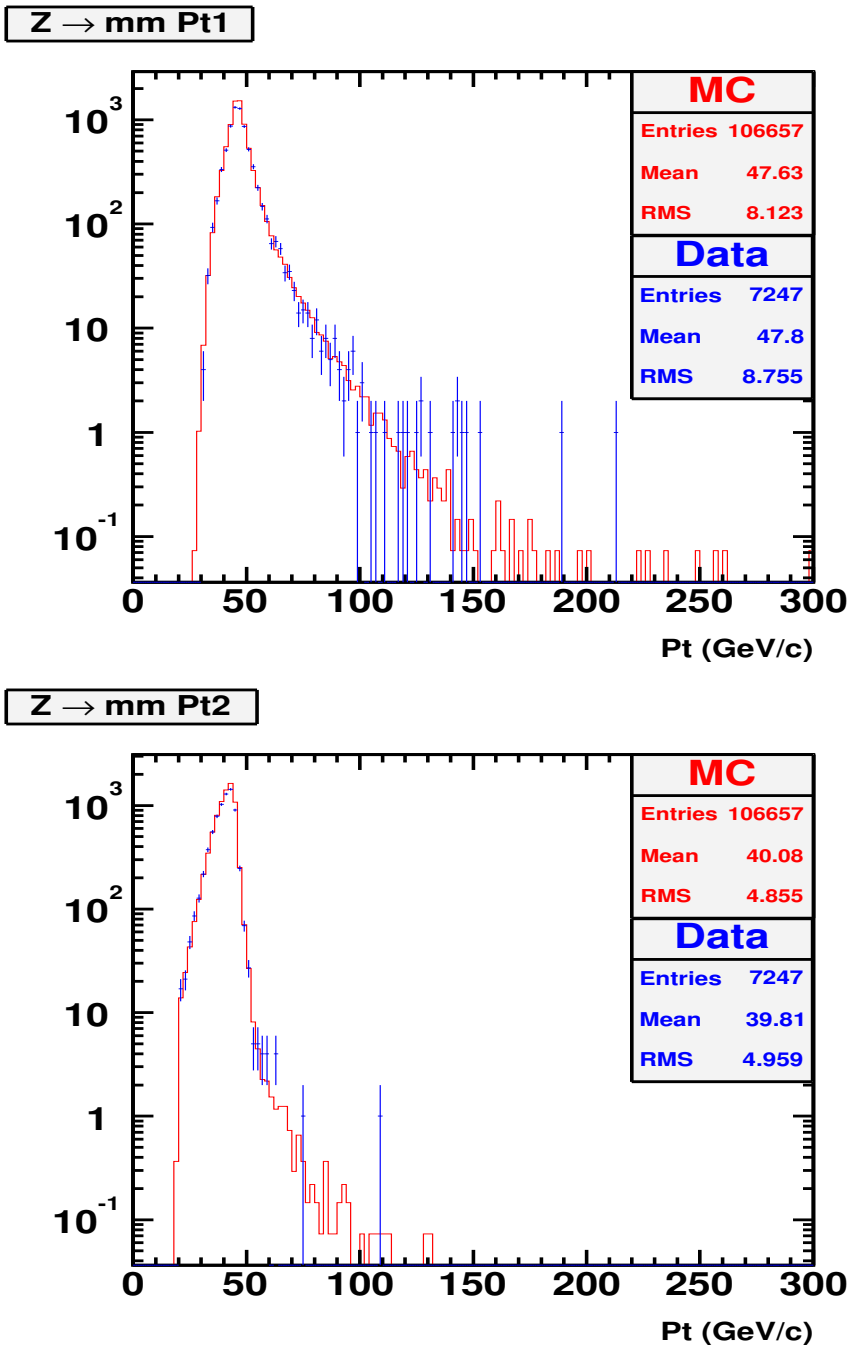

Figure 22: $Z \rightarrow \mu\mu$ P_T.

E $e\mu$ Control Region Kinematics

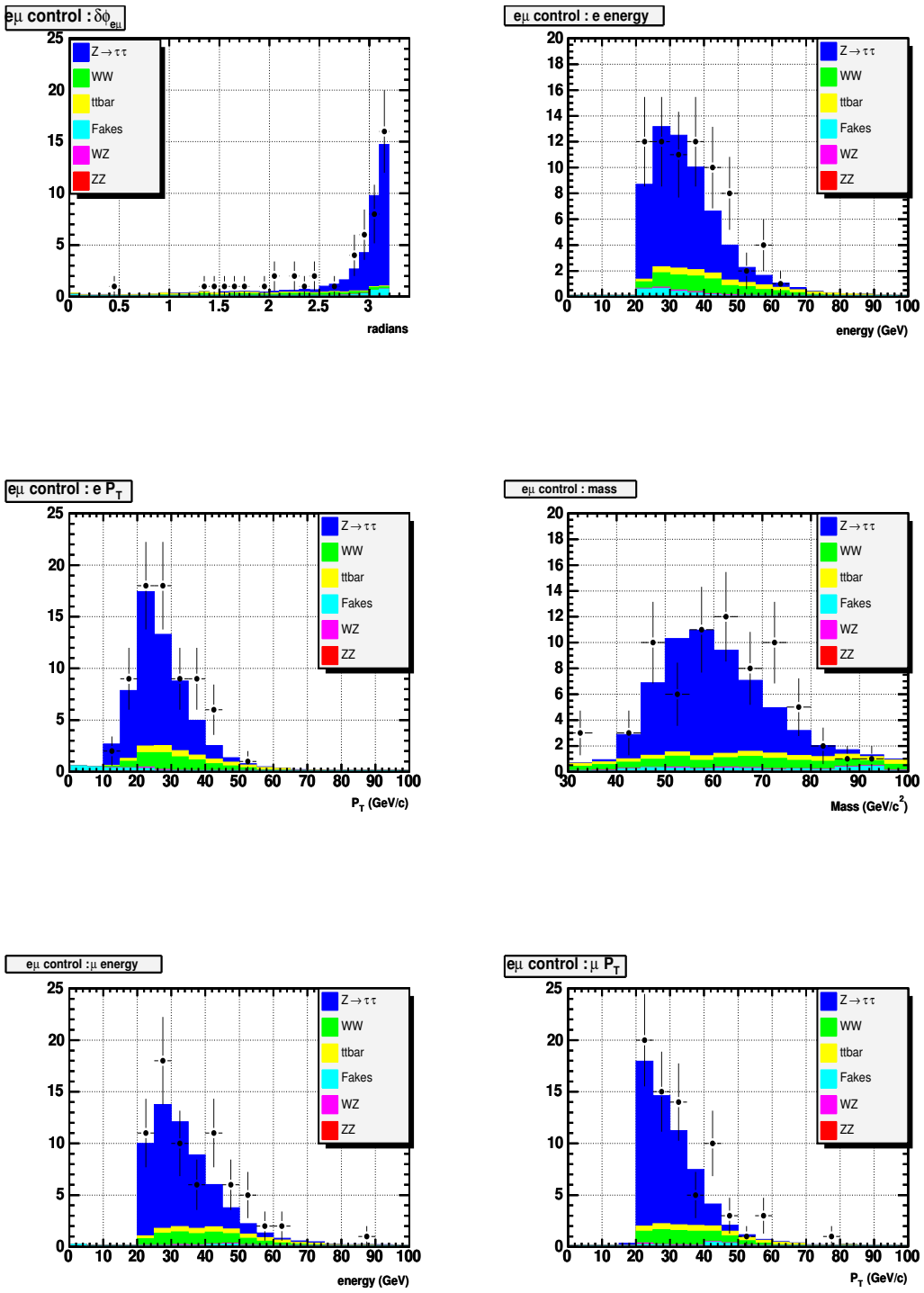

Figure 23: $e\mu$ **Control Region Kinematics.**

F χ^2 Results

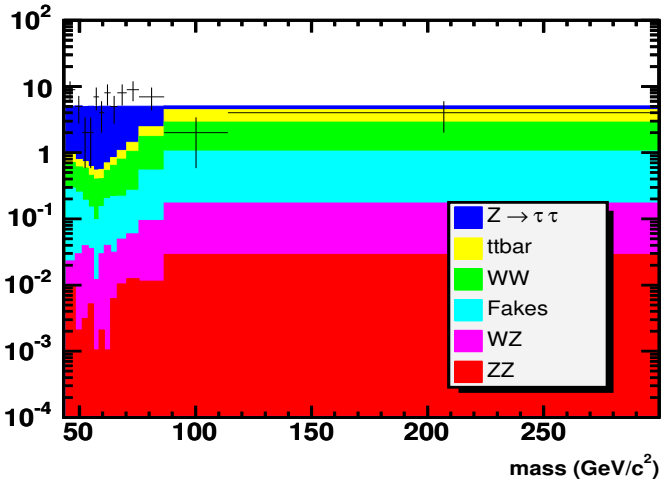

Bin	Upper edge	Expected	Observed	χ^2
1	43.75	5.00 ± 2.24	5	1.10E-06
2	48.15	5.03 ± 2.24	9	3.128
3	51.25	5.10 ± 2.26	5	0.002
4	53.7	5.02 ± 2.24	2	1.816
5	56	5.03 ± 2.24	2	1.829
6	58.4	5.01 ± 2.24	7	0.791
7	60.7	5.03 ± 2.24	4	0.213
8	63.45	5.02 ± 2.24	8	1.763
9	66.35	5.01 ± 2.24	5	5.41E-06
10	70.3	5.05 ± 2.25	8	1.718
11	75.7	5.08 ± 2.25	9	3.035
12	86.5	5.04 ± 2.24	7	0.765
13	114	5.08 ± 2.25	2	1.866
14	1000	5.80 ± 2.41	4	0.561
total reduced χ^2				1.35
p value				0.231

Table 11: Reduced χ^2 Results We calculate a variable bin width χ^2 to determine the consistency of our results with the SM. The p-value for the full distribution excludes the RPV sneutrino hypothesis at the 0.05% significance level.

References

[1] B. Murakami, hep-ph/0110095, "The impact of lepton-flavor violating Z' bosons on muon $g-2$ and other muon observables."

[2] D. Choudhury, S. Majhi and V. Ravindran. "CD Corrections to Resonant Slepton Production in Hadron Colliders".

[3] "A Measurement of the $t\bar{t}$ Cross Section Using Dileptons". CDF6830.

[4] D. Acosta. hep-ex/0307012, 22 October 2003.

[5] Marc Chemtob. hep-ph/0406029, 2 June 2004.

[6] J. Kang and P. Langacker, hep-ph/0412190, "Z' Discovery Limits for Supersymmeteric $E6$ Models".

[7] P. Wintz, in *Proceedings of the First International Symposium on Lepton and Baryon Number Violation.*p 531 (1998).

[8] C. Hill, J. Incandela and C. Mills. "Electron Identification in Offline Release 5.3". CDF Note 7309.

[9] Victoria Martin. "High-p_T Muon ID Cuts and Efficiencies for use with 5.3.1 Data and 5.3.3 MC". CDF Note 7367.

[10] Yoshio Ishizawz and Jason Nielsen. "Trigger Efficiencies for High E_T Electrons". CDF Note 7401.

[11] Jane Nachtman and Michael Schmitt. "The Sliding-qT Ratio Method". CDF Note 7403.

[12] Mircea Coca, Andrew Ivanov, Ricardo Eusebi, Eva Halkiadakis, Andy Hocker, Paul Tipton. "Determination of the Fake Lepton Background for the Summer 2003 Top Dilepton Cross Section Analysis". CDF6742.

[13] S. Klimenko, J. Konigsberg, and T.M. Liss, FERMILAB-FN-0741 (2003).

[14] Joel Heinrich, Craig Blocker, John Conway, Luc Demortier, Louis Lyons, Giovanni Punzi, Pekka K, Sinervo. "Interval estimation in the presence of nuisance parameters. 1. Bayesian approach". CDF7117.

[15] S. Dimopolous. R. Esmailzadeh. L.J. Hall. J.P. Merlo and G. D. Starkman. Phys Rev. D. **41.** 2099 (1990)

[16] http://www.gnu.org/software/gsl/

[17] M. Carena, A. Deleo, B. Dobrescu, T. Tate. "Z' Gauge Bosons at the Tevatron", FERMILAB-Pub-04/129-T (2004).

[18] Chris Hays, Ashutosh Kotwal, Larry Nodulman, Oliver Stelzer-Chilton, William Trischuk, Ian Vollrath. "Measurement of the W Mass". CDF Note 7104.

[19] L. Balka, et al., Nucl. Instr. & Meth. A 267 (1988) 272

[20] http://cdfrh0.grid.umich.edu/m̃iller/pdf/pdf_acceptance.html